

Deep Learning Algorithms to Isolate and Quantify the Structures of the Anterior Segment in Optical Coherence Tomography Images

Tan Hung Pham^{1,2}, Sripad Krishna Devalla¹, Aloysius Ang³, Soh Zhi Da², Alexandre H. Thiéry⁴, Craig Boote^{1,5,6}, Ching-Yu Cheng^{2*}, Victor Koh^{7*}, and Michaël J. A. Girard^{1,2*}

¹*Ophthalmic Engineering and Innovation Laboratory, Department of Biomedical Engineering, Faculty of Engineering, National University of Singapore, Singapore.*

²*Singapore Eye Research Institute, Singapore National Eye Centre, Singapore.*

³*Yong Loo Lin School of Medicine, National University of Singapore, Singapore*

⁴*Department of Statistics and Applied Probability, National University of Singapore, Singapore.*

⁵*School of Optometry and Vision Sciences, Cardiff University, UK.*

⁶*Newcastle Research and Innovation Institute, Singapore.*

⁷*Department of Ophthalmology, National University Hospital, Singapore.*

**All three contributed equally and all three are corresponding authors.*

September 4, 2019

Abstract

Accurate isolation and quantification of intraocular dimensions in the anterior segment (AS) of the eye using optical coherence tomography (OCT) images is important in the diagnosis and treatment of many eye diseases, especially angle closure glaucoma. In this study, we developed a deep convolutional neural network (DCNN) for the localization of the scleral spur, and the segmentation of anterior segment structures (iris, corneo-sclera shell, anterior chamber). With limited training data, the DCNN was able to detect the scleral spur on unseen ASOCT images as accurately as an experienced ophthalmologist; and simultaneously isolated the anterior segment structures with a Dice coefficient of 95.7%. We then automatically extracted eight clinically relevant ASOCT parameters and proposed an automated quality check process that asserts the reliability of these parameters. When combined with an OCT machine capable of imaging multiple radial sections, the algorithms can provide a more complete objective assessment. This is an essential step toward providing a robust automated framework for reliable quantification of ASOCT scans, for applications in the diagnosis and management of angle closure glaucoma.

1 Introduction

By 2020, the number of people affected by primary angle closure glaucoma (PACG) is estimated to be up to 23.4 million[40, 29]. PACG is associated with a high rate of blindness[3, 9] that is up to 5 times greater than primary open-angle glaucoma[25]. Therefore, an early diagnosis followed by effective management strategies is essential to reduce the damage to the optic nerve head tissues that could lead to irreversible vision loss[34]. Early diagnosis is crucial in the Asian population, given the higher prevalence of PACG compared to European and African populations[3, 9, 1].

The diagnosis of PACG is based on the status of the anterior chamber angle (ACA)[33, 21, 31]. While the gold standard for ACA assessment is dark-room indentation gonioscopy[28], the procedure requires direct contact with the eye and is highly dependent on the physicians expertise and the background illumination[28, 39]. This can result in poor reproducibility and diagnostic accuracy. In contrast, anterior segment optical coherence tomography (ASOCT) imaging allows for an objective, fast and non-contact assessment of the ACA in a standardized dark-room environment[39, 19]. However, current technology typically requires the manual identification and marking of the scleral spur location (SSL) (**Figure 1**) by a human grader before ACA measurements such as trabecular iris space area (TISA) and angle opening distance (AOD) can be measured to quantify the anterior chamber angle[4]. The introduction of this subjective human factor has been shown to introduce significant intra- and inter-observer variability[39, 19, 4]. The inconsistent labelling of SSL compromises the diagnosis and the monitoring of treatment effectiveness/disease severity in PACG[4]. In addition, with swept-source ASOCT imaging, there are up to 128 cross-sectional scans obtained per eye. To manually label each individual section in a timely manner would not be clinically viable, and therefore automated image processing algorithms are required.

Deep convolutional neural networks (DCNNs) have been shown to perform well with many medical imaging modalities[5, 6, 30, 13, 16], but their applications in ASOCT imaging are nascent. From the perspective of the current study, there are two relevant applications that can benefit from DCNNs, namely: object localization (for SSL detection) and segmentation (for classifying tissues such as the cornea and the iris). Traditional object detection and localization approaches in DCNNs are mainly based on classification and regression[35]. However, this approach requires a large number of labelled images to achieve robust automation[38]. Moreover, accurate landmark localization is critical for the diagnosis and management of PACG. Hence with limited training data, a traditional regression approach is not ideal in providing a high accuracy prediction. Frequently, in the medical context, it might not be feasible to obtain a large number of labelled images due to limited resources and time. This problem is exacerbated in certain ocular conditions that are relatively less common which may benefit from mass screening such as PACG. In addition, the reduced availability of ASOCT images for eyes with PACG can be attributed to the lack of accessible equipment, cost, and clinical expertise.

In this study, we developed a custom hybrid DCNN inspired from widely used U-Net and full-resolution residual network (FRRnet)[26] for the localization of scleral spur, and the segmentation of the anterior segment structures (iris, corneo-sclera shell, anterior chamber). The hybrid DCNN leveraged the U-Net architecture to simultaneously exploit the local (i.e. tissue texture) and contextual (i.e. tissue spatial arrangement) information and exploited the FRRnet pathway to achieve precise localization. Further, we automatically extracted eight clinically relevant ASOCT parameters from the segmented structures. The aim of the work is to offer a robust and automated framework for the accurate localization of the scleral spur and quantification of the ASOCT structures for enhancing the diagnosis and management of PACG.

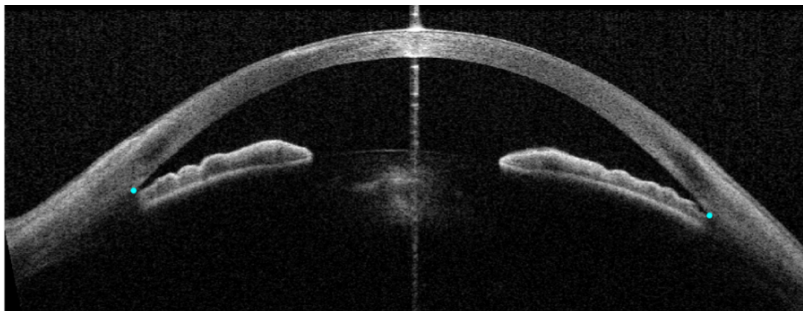


Figure 1: Example of scleral spur location (cyan dots) on a well-centered anterior segment optical coherence tomography scan.

2 Methods

2.1 ASOCT imaging

We included ASOCT images from patients examined at the Eye Surgery Centre, National University Hospital, Singapore. Prior informed consent was obtained for all patients. The study was conducted in accordance with the tenets of the World Medical Associations Declaration of Helsinki and had ethics approval from the National Healthcare Group Domain Specific Review Board. In total, ASOCT images from 100 patients (175 eyes) were included for analysis. The scans were obtained from the swept-source Casia SS-1000 ASOCT (Tomey Corporation, Nayoga, Japan). For each eye, a 360-degree scan yielded up to 128 cross-sections of the anterior segment. We used 620 images from 42 patients (75 eyes) for training and another 200 images from a further 58 patients (100 eyes) for testing. Since each image contained two scleral spur instances, we further divided the images in half for scleral spur localization (**Figure 2**).

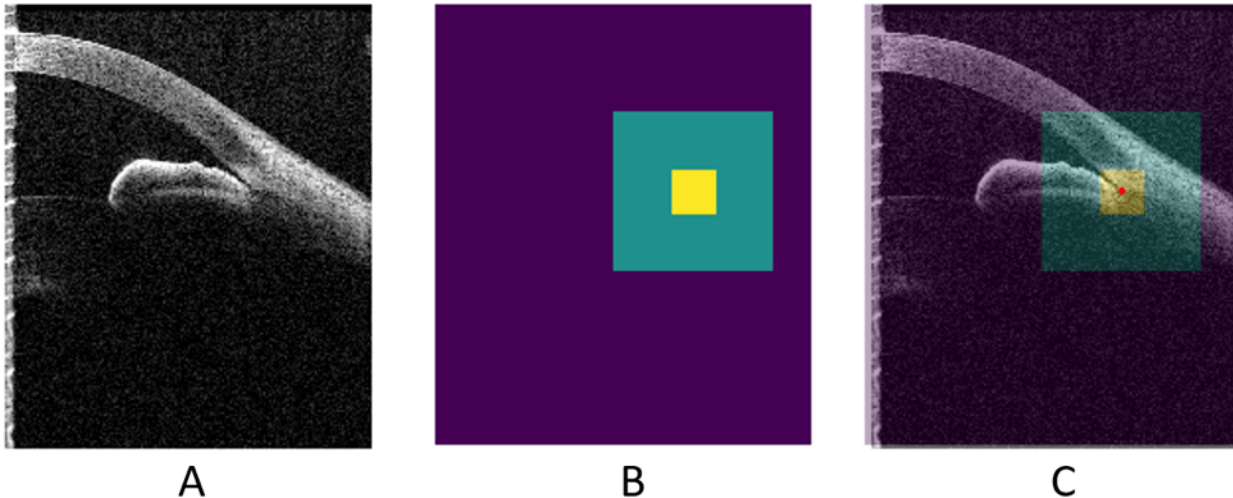


Figure 2: Labeled data for the SSL. (A) Input ASOCT image; (B) ground truth of the SSL (yellow represents focus region, cyan represents attention region) and (C) prediction of the SSL with red dot as the center of focus region.

2.2 Small landmark localization and ASOCT segmentation

The accurate localization of small landmark points using neural networks has always been challenging[44]. In the current study, we adopted a segmentation approach for both the landmark localization and the ASOCT segmentation. A MATLAB (R2018a, MathWorks Inc., Natick, MA) script was prepared to assist in labelling the SSL (landmark localization). Three definitions were used to locate the scleral spur: **1**) A change in curvature in the corneo-scleral interface; **2**) The posterior end of the trabecular meshwork; and **3**) The posterior end of a protruding structure along the cornea and sclera[4, 32]. In each image, the following classes were identified (**Figure 2**): **(1)** focus region (in yellow); **(2)** attention region (in cyan); and **(3)** the background (in purple).

FIJI[15] was used to obtain the manual segmentations of the ASOCT tissues. In each image, the following classes were identified (**Figure 3**): **(1)** the iris (in red);**(2)** the corneo-sclera shell (in blue); **(3)** the anterior chamber (in green); and the background (in black). The SSL labelling and the manual segmentations used for training the DCNNs were prepared by two trainers: a trained medical student (AA), and a trained observer (THP), both with more than two years of experience in ASOCT imaging.

The landmark localization and segmentation performance of the DCNNs on unseen ASOCT images were evaluated by three graders: the aforementioned trained observer (observer A; THP) and medical student (observer B; AA), and a glaucoma fellowship trained ophthalmologist (observer C; VK) with eight years of experience in the management of PACG.

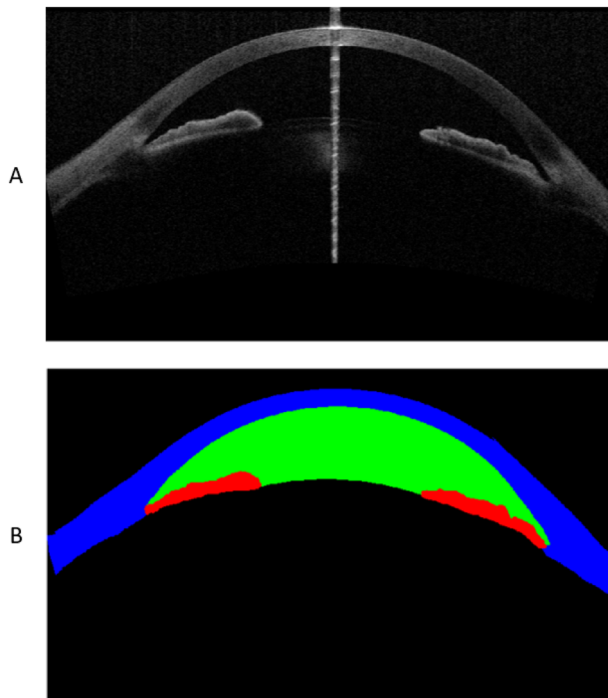


Figure 3: Labelled data for ASOCT segmentation. **A**: input image. **B**: ground truth for output, red: iris, blue: corneo-sclera shell, green: anterior chamber.

2.3 Measurement of ASOCT parameters

The ASOCT parameters could be automatically measured once the scleral spur was defined and the anterior segment intraocular tissues segmented. The key structural parameters, including ACA, anterior chamber and iris-based measurements were automatically computed based on their definitions **Table 1**.

2.4 Network architecture and training

In recent years, several research groups have successfully used U-Net and its variants[45, 16, 11, 30] in medical image segmentation. The sequential downsampling and upsampling of images combined with skip connections[7] help in simultaneously extracting both the local (i.e., tissue texture) and contextual (i.e., tissue spatial arrangement) information. This allows U-Net style architectures to achieve very high levels of segmentation accuracy even when trained with limited training data[30, 16]. Another promising but less explored DCNN in medical imaging applications is the FRRnet[26]. The network has two pathways: a full resolution path that helps in identifying precise boundaries and a multi-scale feature extraction pathway that is responsible for robust feature recognition. Also, the residual connections improve the gradient flow through the network[14]. By combining the information from both the pathways, the FRRnet was able to achieve precise localization and robust feature recognition[26].

Many studies have demonstrated that an ensemble network that learned to combine the predictions of multiple DCNNs into a single predictive model offered a better accuracy than each of the networks separately[12, 18]. When trained on the same training data as the individual DCNNs (weights of the individual DCNNs were frozen), the ensemble network learned to reduce the variance for each network, thus dramatically increasing the predictive power.

In this study, we developed FRRU-Net (full resolution residual U-Net), a hybrid DCNN that exploited the inherent advantages of both the U-Net and the FRRnet. For the detection of the SSL, the FRRU-Net was used, while an ensemble of the U-Net, FRRnet, and the FRRU-Net was used for the segmentation of the ASOCT structures [Figure 4, Figure 5, Figure 6, Figure 7].

All three networks were trained end to end using an Adam optimizer and categorical cross entropy loss function[38] with a learning rate of 0.00005. All the convolution layers were activated with a leaky rectifier linear unit (ReLU)[43] activation function. A dropout layer with a probability of 0.5 was used after every building block to reduce the overfitting. Given the limited size of the training dataset, the DCNNs variance was increased through data augmentation techniques such as rotation, width shift, height shift, shear, zoom, flip, brightness and contrast shift. The final U-Net, FRRnet, FRRU-Net, and the ensemble network consisted of 7.80 M, 4.2 M, 4.2 M, and 1.7K trainable parameters respectively. All networks were trained and tested on an NVIDIA GTX 1080 founders edition GPU with CUDA v8.0 and cuDNN v5.1 acceleration. Using the given hardware configuration, for each ASOCT image the network was able to detect the SSL in 0.108 ± 0.0035 seconds and segment the ASOCT tissues in 0.324 ± 0.0018 seconds. The parameters were then automatically computed on a CPU (Intel Xeon at 2.1 GHz) in under 1.723 ± 0.287 seconds. It should be noted that parameter measurement can be accelerated by parallelism since each scan is independent.

Table 1: **Definitions of important anterior segment optical coherence tomography parameters.**

Parameter	Definition
Anterior Chamber Depth (ACD)	Axial distance between corneal endothelium to anterior lens surface[8]
Lens Vault (LV)	Perpendicular distance from middle of the line connecting the scleral spurs to the anterior pole of the lens[22]
Anterior Chamber Width (ACW)	Distance between two scleral spurs[23]
Anterior Chamber Area (ACA)	Area bordered by posterior surface of the cornea, anterior surface of iris and anterior surface of the lens[42]
Angle Opening Distance (AOD)	Distance between the anterior iris surface and posterior corneal surface on a line perpendicular to the trabecular meshwork, a distance from the scleral spur (500 μm , 750 μm , etc.)[41]
Trabecular Iris Space Area (TISA)	Area of a trapezoid created by the following boundaries: AOD of a distance from scleral spur (500 μm , 750 μm , etc.), line from scleral spur perpendicular to plane of inner scleral wall to the iris, inner corneoscleral wall, iris surface[41]
Iris thickness (IT)	IT at a distance from the scleral spur or a relative distance in the iris (eg: middle of iris)[37]
Iris Curvature	Distance from iris greatest convexity point to the line between most central and most peripheral iris pigment epithelium[37]

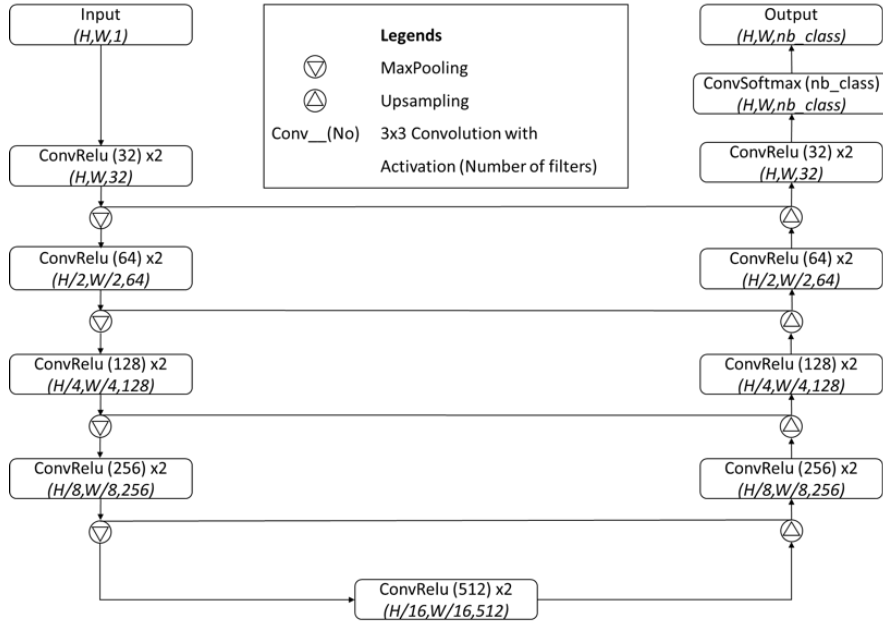


Figure 4: U-net architecture.

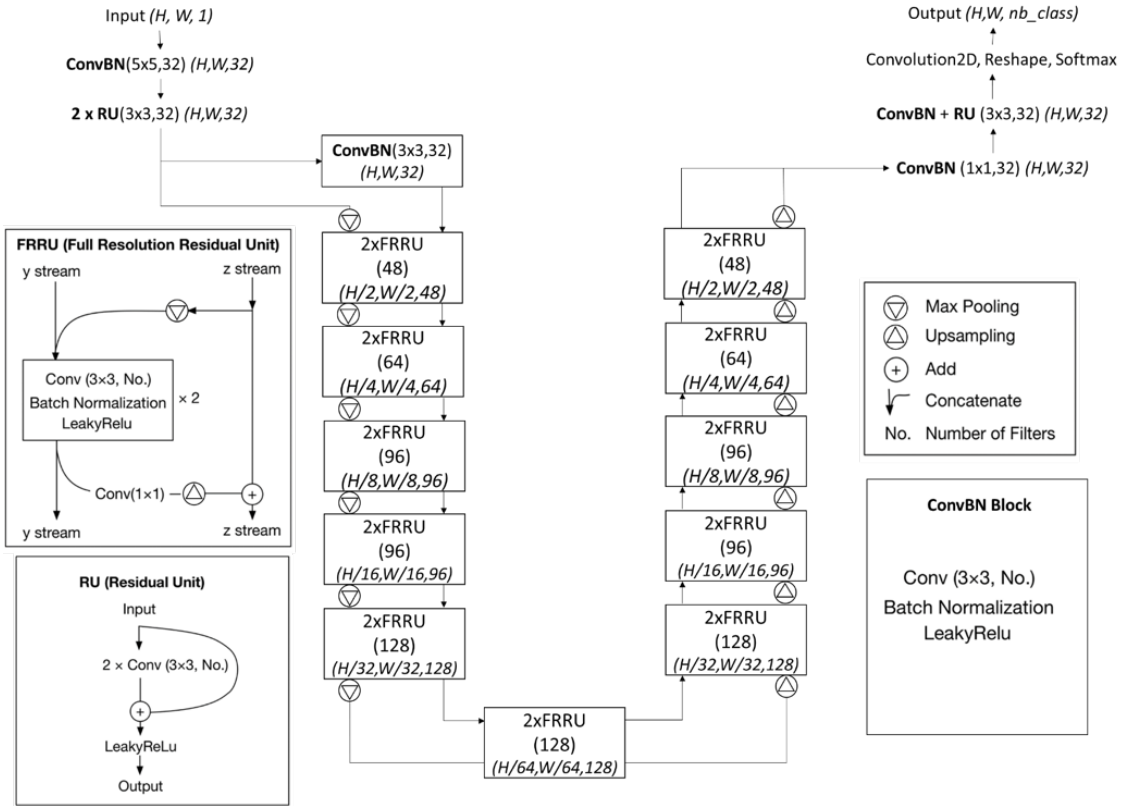


Figure 5: FRRN architecture.

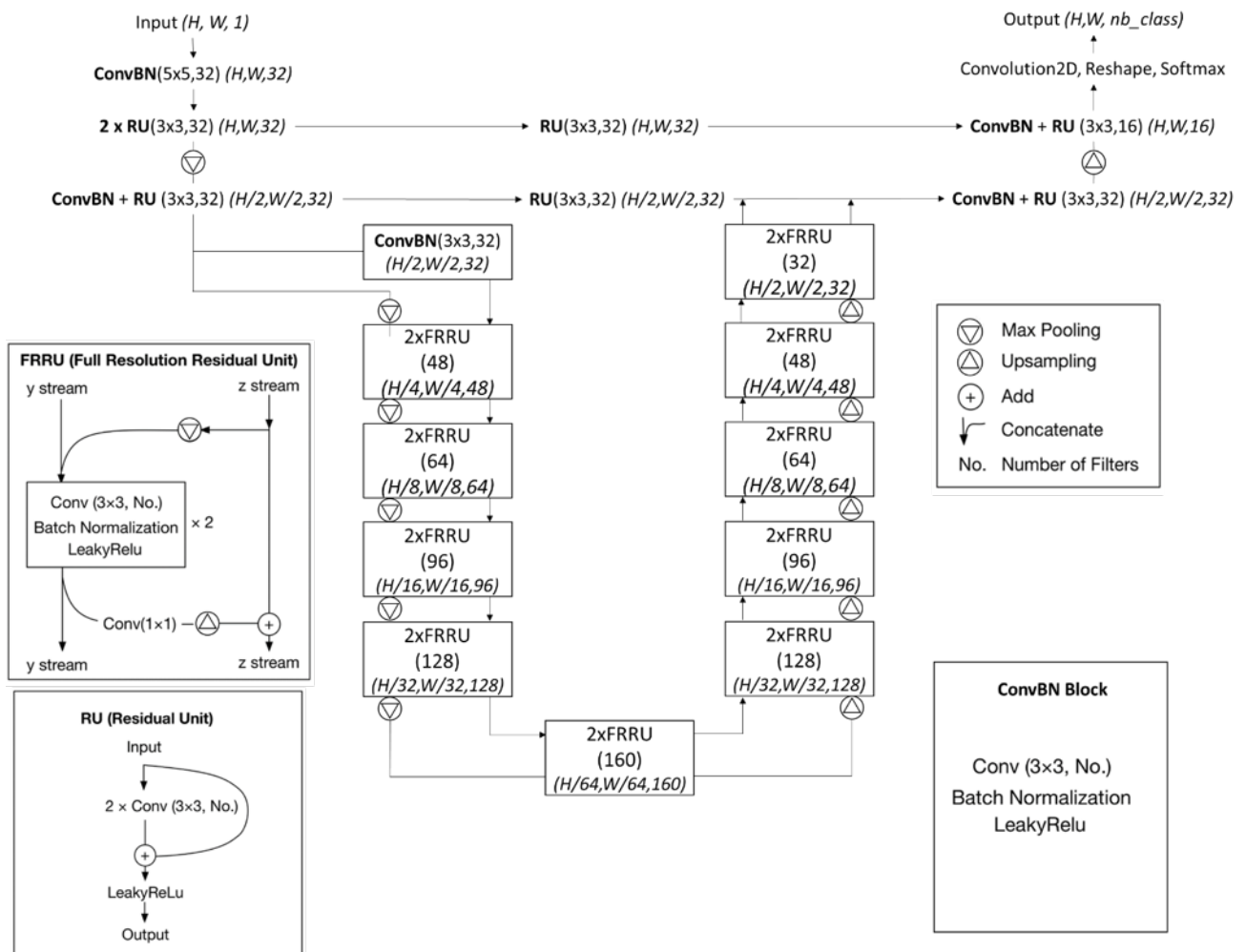


Figure 6: Proposed Network: Hybrid between U-net and Full Resolution Residual Net FRRU-net.

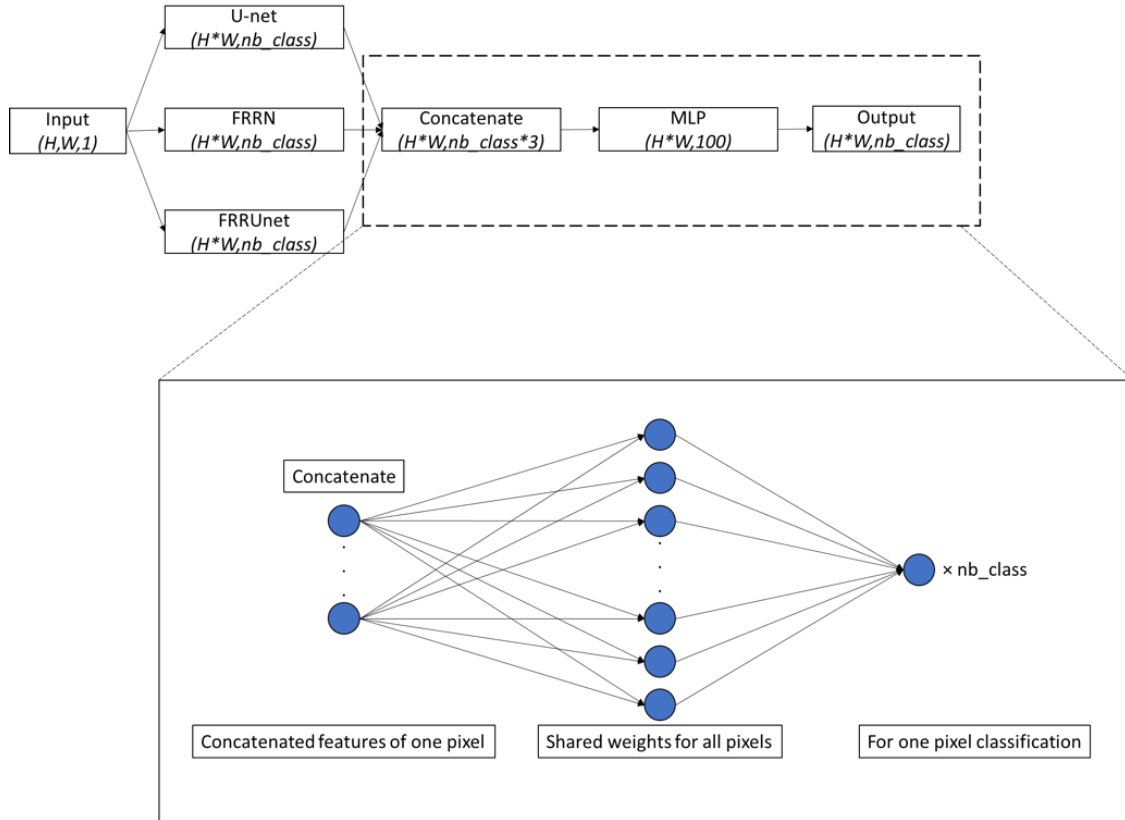


Figure 7: Ensemble architecture that combine the three base models.

2.5 Inter and intra observer tests

We performed an inter-observer agreement test to assess the reproducibility when identifying the scleral spur between three human observers: A Trained non-expert, B Trained medical student; C Fellowship-trained glaucoma expert well-versed in ASOCT analysis and the software algorithm. The intra-observer agreement test assessed the extent of repeatability among the human observers and their comparison with the software algorithm. A paired t-test was used to measure the extent of agreement on-average and Bland-Altman plots were used to depict the limit of agreement (± 1.96 SD) and the distribution of discrepancy between individual measurements. The intra-correlation coefficient (ICC), assessed with a single rater, absolute agreement, two-way random effect model, was used to reflect the degree of agreement and correlation between measurements. ICCs of < 0.50 , $0.50-0.75$, $0.75-0.90$; < 0.90 were taken as poor, moderate, good and excellent measures of reliability, respectively. All p-values presented are 2-sided and statistically significant if < 0.05 .

2.6 Quality check

Poor quality scans (low signal strength, presence of motion/blink artefact, improper head positioning etc.) can affect the localization and segmentation performance of the DCNNs, thus resulting in incorrect automated measurements. In this study, we performed a two-step automated quality check based on the predictions obtained to eliminate poor quality ASOCT images. First, upon the detection of the SSL a square region surrounding the center of the predicted region was obtained as the reference. A confidence index was computed as the intersection over union (IoU; between 0-1) between the predicted and reference regions. Scans that yielded a confidence index greater than or equal to 0.80 were considered good, while lower values

were designated as poor quality. Second, for the segmentation the number of closed and continuous contours representing each class were used to assess the quality of a scan, i.e., the iris should have two contours, while the corneo-sclera shell and the anterior chamber should have only a single contour each. Scans with predictions that did not satisfy these criteria were considered as poor quality. Finally, the automatically extracted parameters were considered reliable only if the ASOCT scan satisfied both the aforementioned quality check criteria. The test images are made sure to be of usable quality clinically.

3 Results

All results in this section are from 4 observers: A – trained non-expert, B – trained medical student, C – fellowship-trained glaucoma expert well-versed in ASOCT analysis, M – Trained machine. The same denotation is used throughout. The mean age of the patients was 62.20 ± 8.35 and 31.91% of them were males. The percentage for Chinese, Malay, Indian and other races was 77.86%, 11.42%, 7.86% and 2.86% respectively.

3.1 Scleral spur localization

First, our proposed segmentation approach was compared against a regression approach, both utilizing DC-NNs. The final models were trained for 1,000 iterations and then tested against 3 human observers **Figure 8 A**. The segmentation approach was closer to human observers for all cases. The next test showed that our segmentation approach could reach human level detection with a much smaller training dataset (~ 200 samples or ~ 100 images) **Figure 8 B**.

Inter-observer tests showed that human grader differences were not significantly different from human and machine differences in most cases **Figure 9 A**. Moreover, intraclass correlation (ICC) was done for each observer pair for the X and Y coordinates of the scleral spur location **Table 2**. It was shown that the machines scleral spur marking was in high agreement with human graders. Bland-Altman plots for Machine – Human pair was further provided in **Figure 10**.

Table 2: ICC results for Inter Observer Test

Two-way Single Score Absolute Agreement ICC									
X Coordinate	A	B	C	M	Y Coordinate	A	B	C	M
A	1	0.978	0.985	0.984	A	1	0.993	0.995	0.994
B		1	0.983	0.979	B		1	0.994	0.993
C			1	0.984	C			1	0.993
M				1	M				1

The machine neural network was deterministic once training was complete, meaning that a given input always resulted in the same output. Hence, to do intra-observer tests, another model was trained from scratch and used to compare with the first model. RMS difference for the machine intra-observer test was significantly smaller than most human intra-observer tests (except for observer A, whose intra-observer result was similar to the machine)(**Figure 9 B**). This means that machine SSL prediction generally had lower variability than that of human grader.

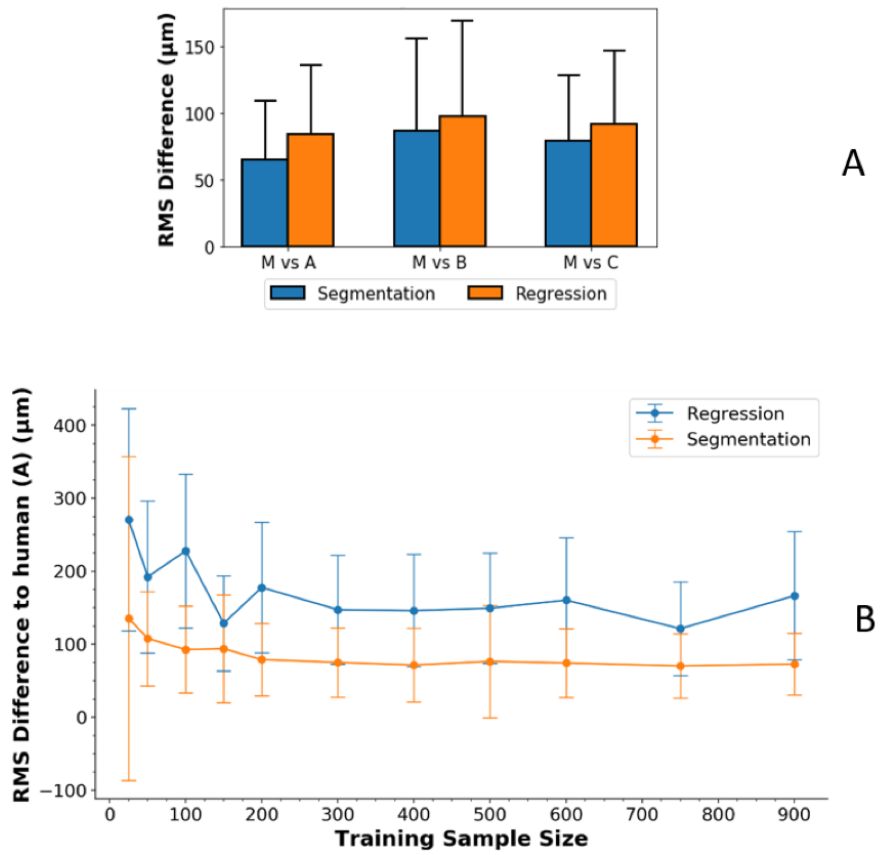


Figure 8: Segmentation vs Regression Approach. **A:** Inter-observer test against human observers. **B:** Varying training sample size and calculated distance against human observer.

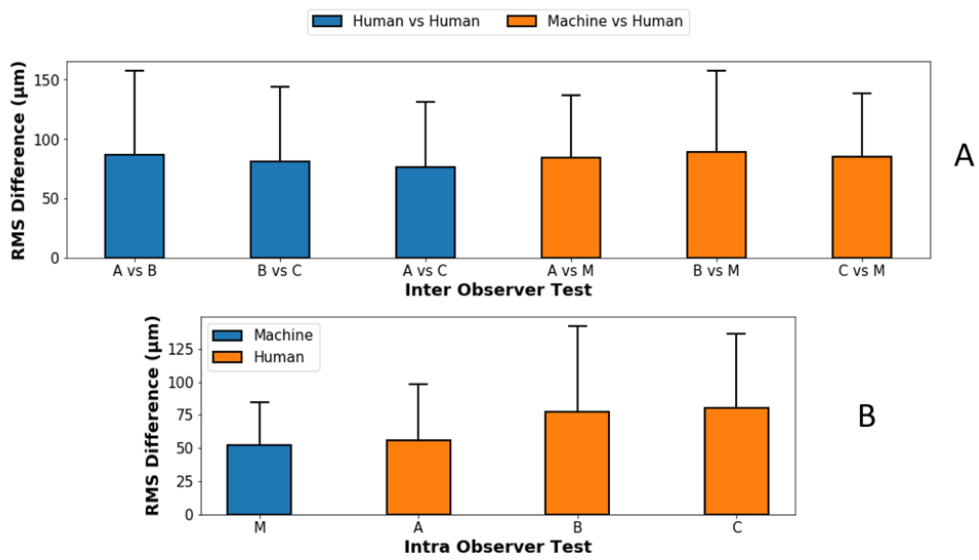


Figure 9: Observer Test results. **A:** Inter-observer Test. **B:** Intra-observer Test.

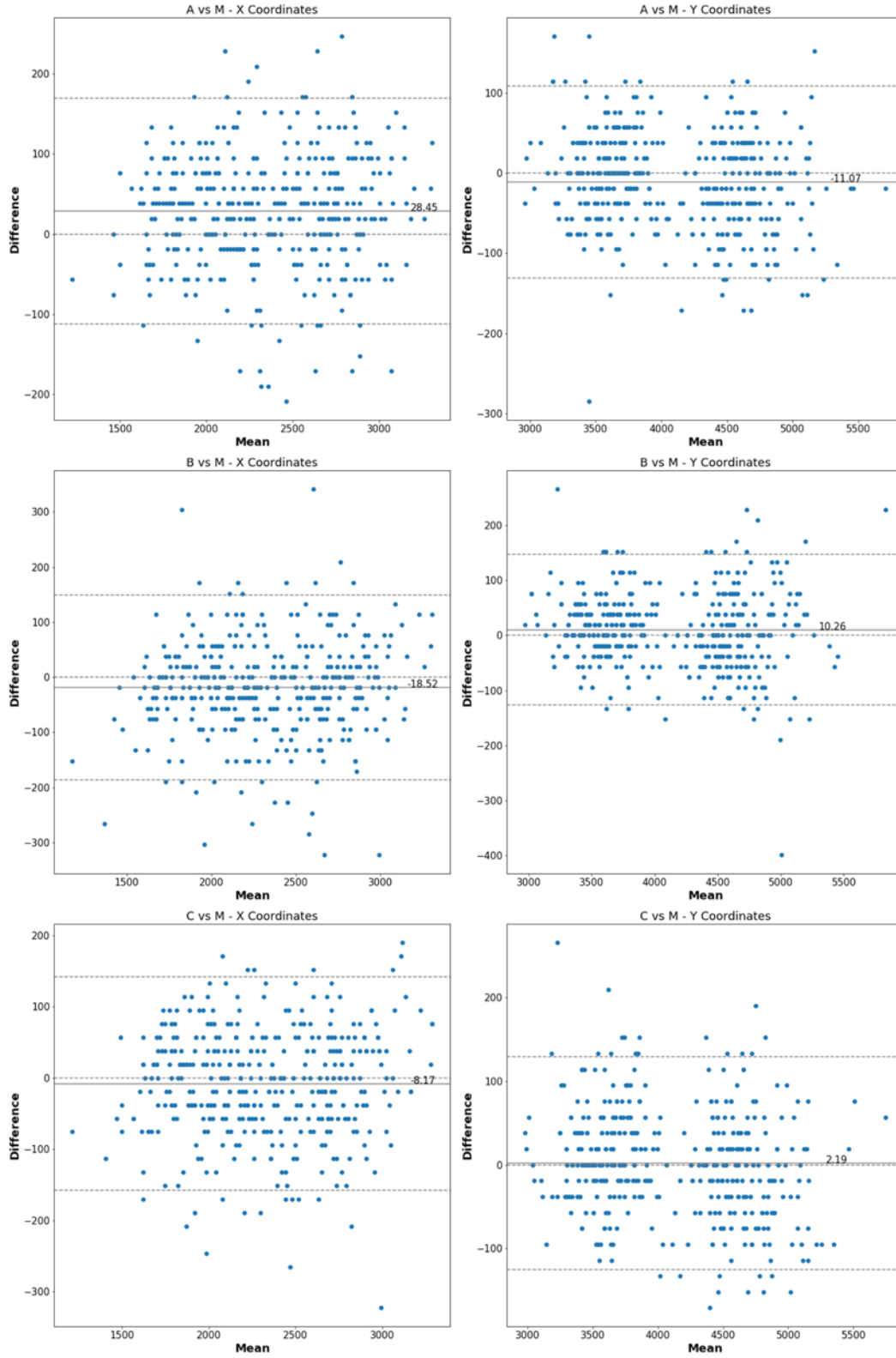


Figure 10: Bland-Altman Plot for Human-Machine Inter Observer Test, both axes measured in μm .

3.2 ASOCT segmentation

The ASOCT segmentation performance of the trained network was validated using the Dice coefficient, sensitivity and specificity **Figure 11**, as described below. The Dice coefficient was used to assess the similarity between the manual segmentation and DCNN segmentation. The coefficient was defined between 0 and 1 (0: no overlap; 1: perfect overlap), and was calculated for each class as follows:

$$\text{Dice score} = \frac{2 \times |D \cap M|}{2 \times |D \cap M| + |D \setminus M| + |M \setminus D|}$$

where D and M are the set of pixels representing the particular class in the DCNN and manual segmentation, respectively.

Specificity and sensitivity were used to obtain the true negative (assess false predictions) and true positive rates (assess correct predictions) respectively. They were defined for each class as follows:

$$\text{Specificity} = \frac{|\bar{D} \cap \bar{M}|}{|\bar{M}|}$$

$$\text{Sensitivity} = \frac{|D \cap M|}{|M|}$$

Both specificity and sensitivity were defined between 0 and 1. Examples of machine segmentation results can be found in **Figure 12**.

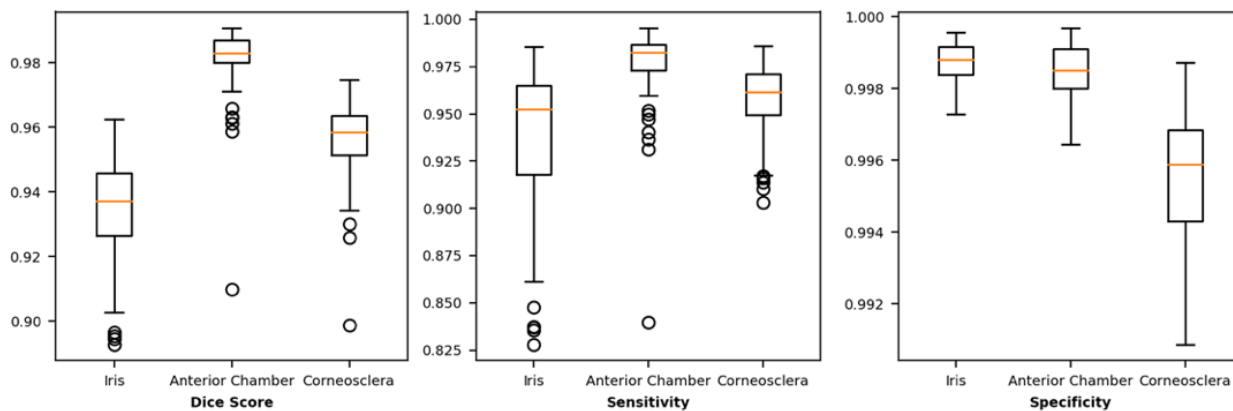


Figure 11: Validation scores for ASOCT segmentation.

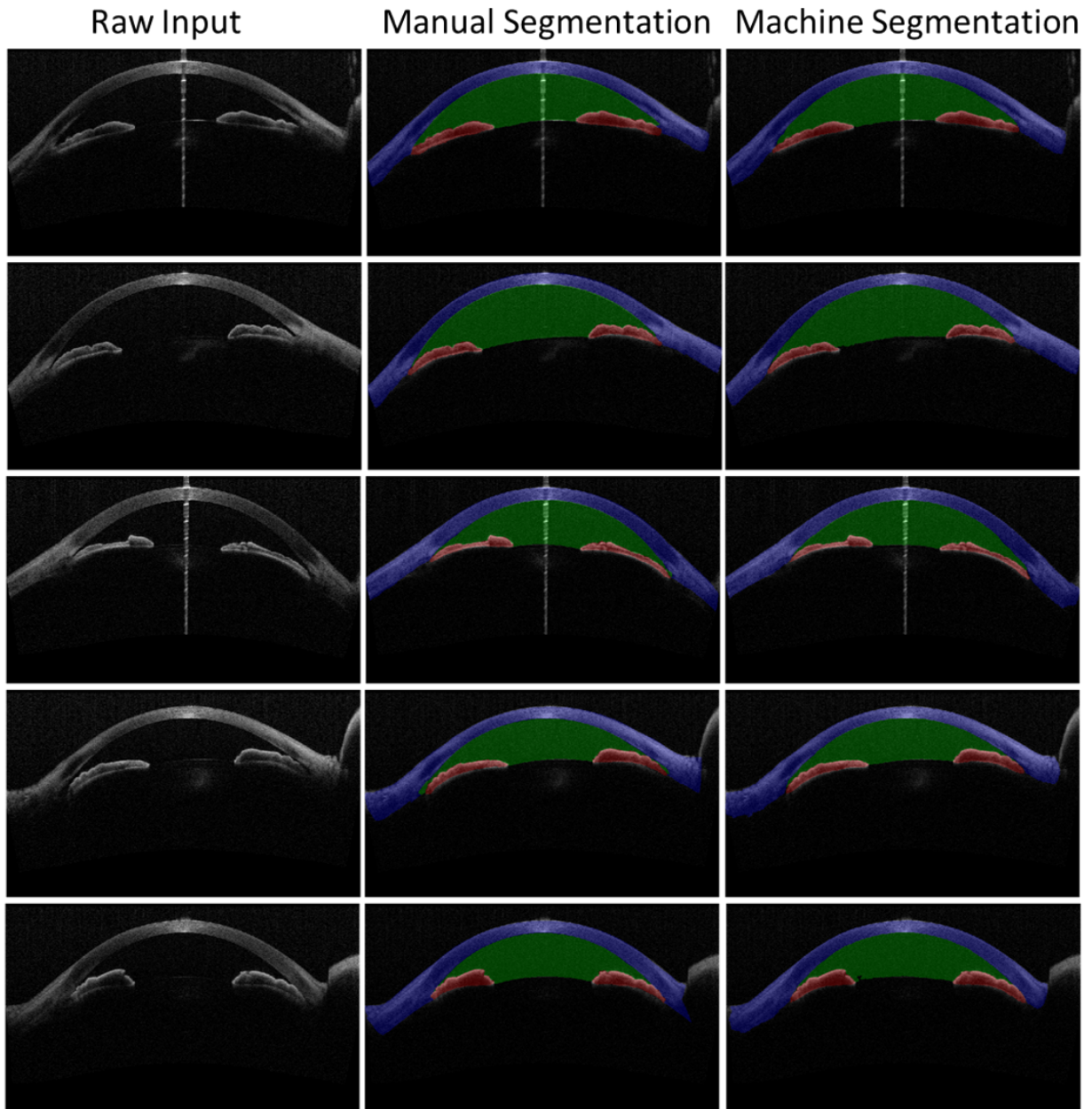


Figure 12: Example predictions on test set versus human manual segmentation.

3.3 Parameter extraction

Parameter extraction was a crucial step to help validate the scleral spur localization. The segmentation used in this step was fully automated, based on the assumption that the accuracy of automated ASOCT segmentation is already high. **Figure 13** defined the measured ACA parameters. **Table 3** shows ICC results for inter- and intra-observer test agreement. Inter-observer test results showed good to excellent agreement between observers, especially between machine and human. Moreover, for measurements with relatively lower ICC between machine and human, the human-human counterpart results were similar. Intra-observer test ICC for machine was higher than human, indicating that the machine was more consistent and stable.

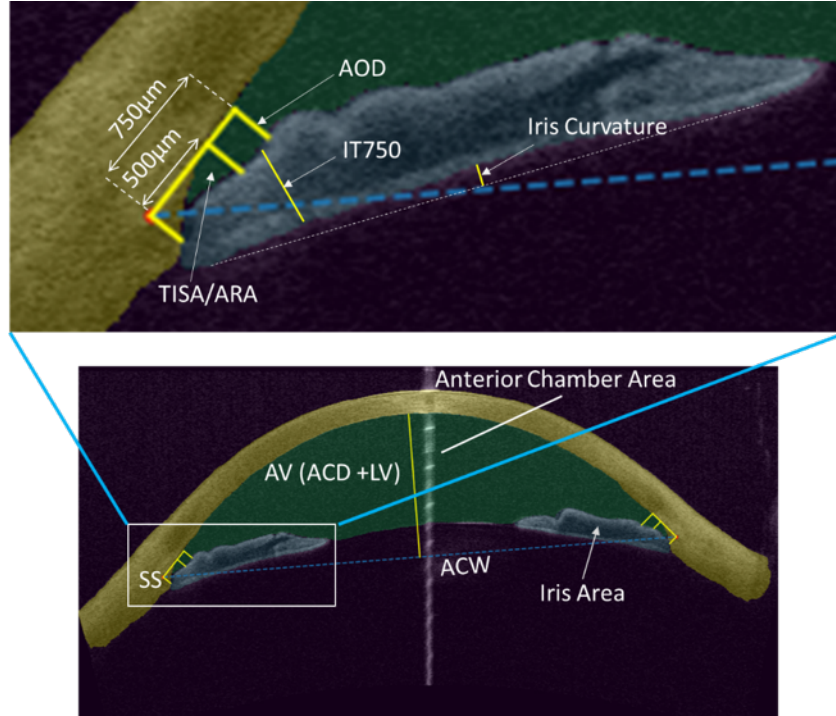


Figure 13: ASOCT Parameter Extraction and Definitions. **Anterior Chamber Depth (ACD)**: axial distance between corneal endothelium to anterior lens surface. **Lens Vault (LV)**: perpendicular distance from the middle of the line connecting the scleral spurs to the anterior pole of the lens. **Anterior Chamber Width (ACW)**: distance between the two scleral spurs. **Anterior Chamber Area (ACA)**: the area bordered by posterior surface of the cornea, anterior surface of iris and anterior surface of the lens. **Angle Opening Distance (AOD)**: distance between the anterior iris surface and posterior corneal surface on a line perpendicular to the trabecular meshwork, at a specific distance from the scleral spur (500 μm , 750 μm etc.). **Trabecular Iris Space Area (TISA)**: area of a trapezoid created by the following boundaries: AOD of a distance from scleral spur (500 μm , 750 μm etc.), line from scleral spur perpendicular to plane of inner scleral wall to the iris, inner corneoscleral wall, iris surface. **Iris thickness (IT)**: IT at a distance from the scleral spur or a relative distance in the iris (eg: middle of iris). **Iris Curvature (ICurve)**: distance from iris greatest convexity point to the line between most central and most peripheral iris pigment epithelium.

Table 3: ICC results for Inter and Intra Observer Tests for ASOCT parameter extraction for ACW, TISA and AOD

Inter Observer Test (Two-way, single score, absolute agreement ICC)				
	A vs M	B vs M	C vs M	A vs B vs C
ACW	0.941	0.931	0.949	0.937
TISA500	0.784	0.722	0.710	0.759
TISA750	0.822	0.728	0.761	0.793
AOD500	0.910	0.902	0.927	0.926
AOD750	0.880	0.863	0.898	0.903
Intra Observer Test (Two-way, single score, absolute agreement ICC)				
	M	A	B	C
ACW	0.979	0.951	0.953	0.954
TISA500	0.847	0.845	0.728	0.646
TISA750	0.884	0.887	0.738	0.702
AOD500	0.959	0.958	0.923	0.881
AOD750	0.948	0.956	0.874	0.901

3.4 Results visualization and quality check

This was assessed visually by exporting the software prediction into an image format. The machine was able to visualize the per-scan results **Figure 14 A**. Moreover, fully automated measurement enables 360° analysis, for example of AOD and TISA **Figure 14 B and C**. The goniogram showed that the inferior quadrants angle is narrower than other quadrants of that specific patient's eye **Figure 14 B and C**. Indicating that a global assessment would provide a more accurate diagnosis.

For image quality check, the ASOCT scans need to pass both the SSL confidence and ASOCT segmentation quality assessment. The SSL confidence can be visualized in 360° as shown in **Figure 15 A**. Visually comparison of good **Figure 14 A** and failed **Figure 15 B and C** cases determined that, if the image quality is good, the SSL confidence should be above 0.85. Accordingly, the SSL confidence threshold was set to 0.8, in order to have some margin from 0.85, meaning scans with SSL confidence below 0.8 were excluded. Moreover, this threshold can be manually adjusted. A failed SSL detection can be seen in **Figure 15 B** on the left scleral spur, where SSL confidence is accordingly very low. For ASOCT segmentation, the exclusion criteria are for iris, anterior chamber, corneo-sclera, a number of contours larger than 5, 6 and 10, respectively. Ideally, the number of contours for the said areas of interest should be 2, 1 and 1 respectively. However, for narrow angle cases and many other noisy cases, there might be insignificant wrong small contours. Hence, we increased the threshold. All of these are hyper-parameters and can be tuned. A future systematic study of hyper-parameter tuning is planned. A failed ASOCT segmentation can be seen in **Figure 15 C**. All failed scans were excluded from the final parameter extraction.

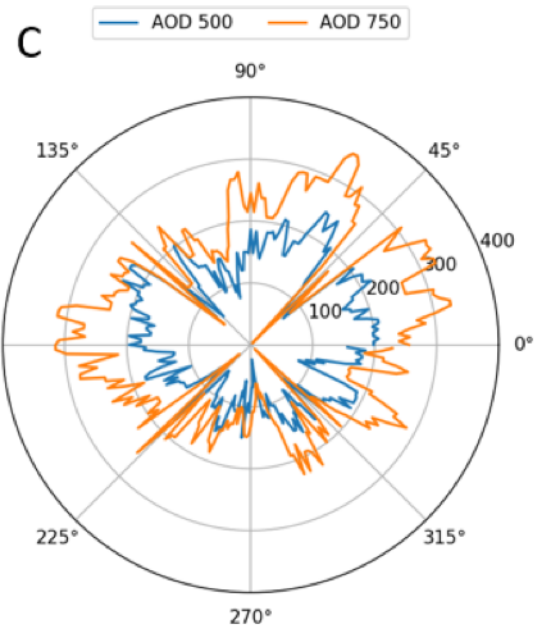
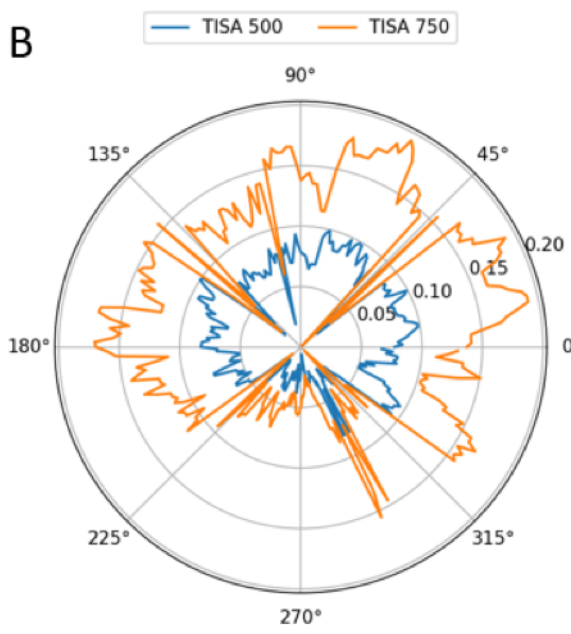
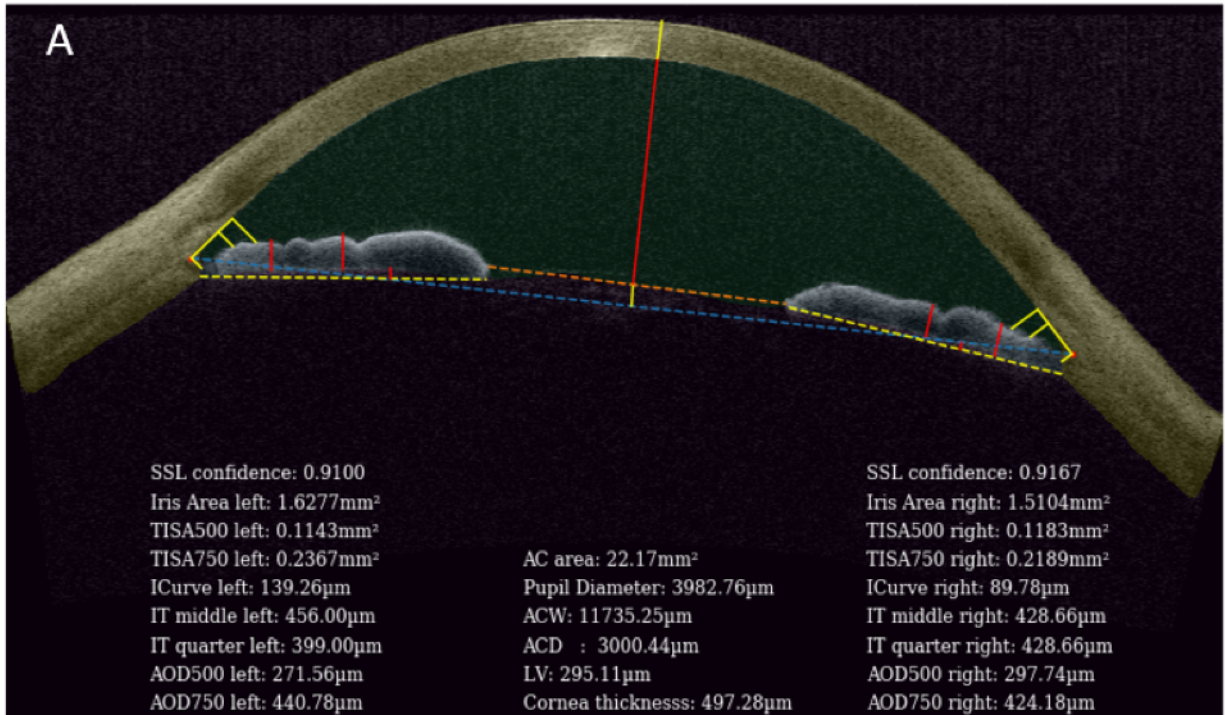


Figure 14: Example of automated results. **(A)** Example parameter measurement of a single scan. **(B)** Example of 360° analysis for AOD. **(C)** Example 360° analysis for TISA. The measured value for each scan in the whole volume is denoted by the radius, while the angle corresponds to the scan position in the ASOCT volume.

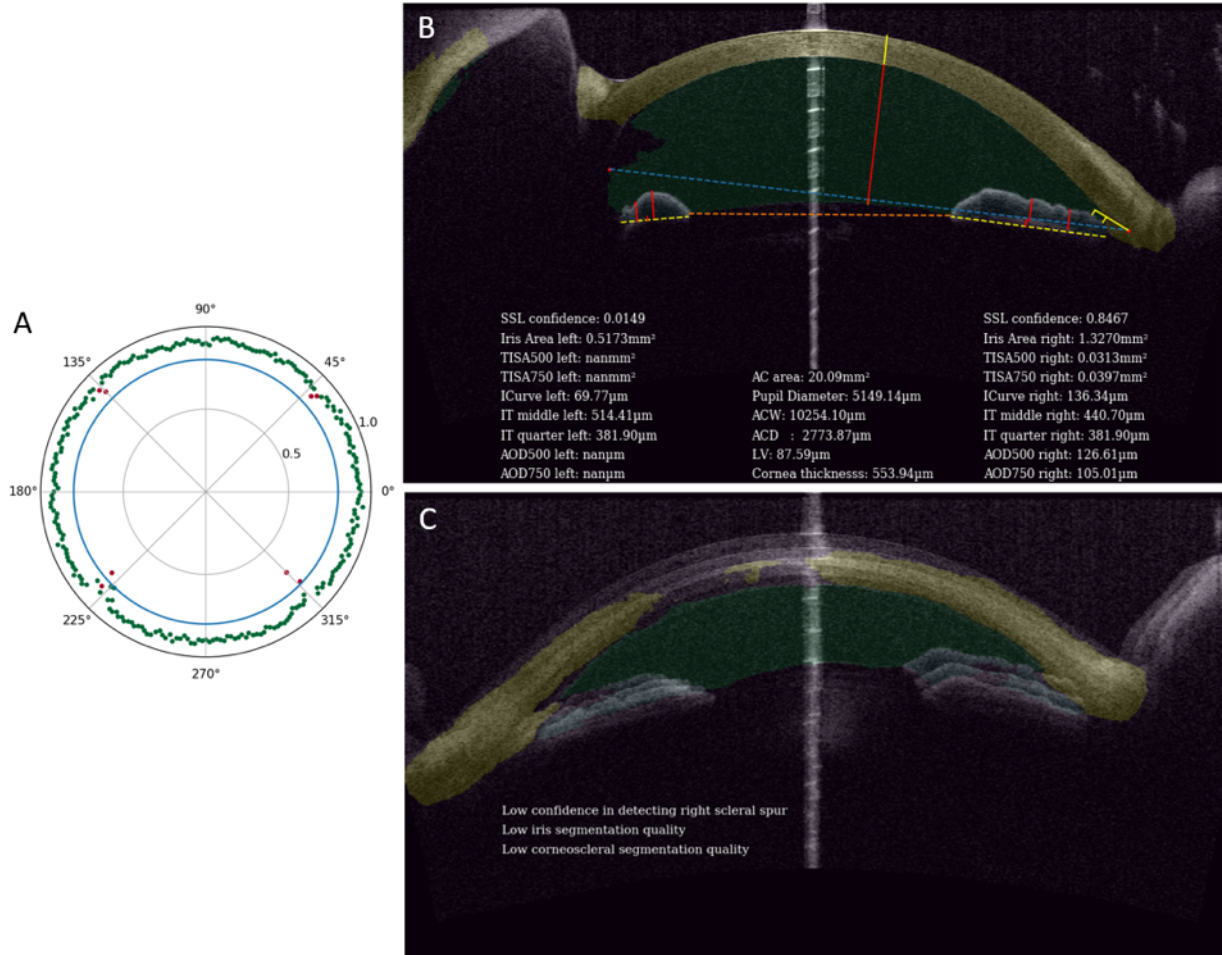


Figure 15: Example of quality check results. **(A)** Visualization of SSL confidence 360°. Greens are passed scans. Reds are failed scans. Blue circle is 0.8 SSL confidence threshold. Red dots above the thresholds are scans that failed the ASOCT segmentation check. In this example 4/128 scans are disqualified. **(B)** Excluded scan due to low SSL confidence on the left side. **(C)** Excluded scan due to bad segmentation quality.

4 Discussion

The use of ASOCT for the assessment of the ACA in angle closure glaucoma is increasingly popular in the clinical setting. However, the practicality and efficiency of its assessment remains challenging for the ophthalmologists. In the absence of an absolute ground truth for SSL, any prediction, including that of experienced human graders, may be expected to contain errors and show variability in performance. The errors consist of bias, variance and irreducible error (noise)[36, 10]. Thus, when a machine learns from human graders, it also learns the humans error. However, with more trainers and data, the errors would be centered around zero[36, 2]. In addition, if the algorithm is developed using expert trainers inputs, these errors would stabilize faster. In clinical practice, errors and variability in SSL on ASOCT scans have huge impact in the diagnosis of angle closure glaucoma because incorrect identification of SSL can result in misdiagnosis and management of patients with PACG. ASOCT imaging has been shown to be more objective and quantifiable compared to gonioscopic techniques[21, 19, 2, 27]. The ACA measurements from ASOCT scans are heavily dependent on the SSL and ophthalmologists gauge treatment effectiveness based on ASOCT measurements

before and after treatment.

One of the strengths of the presented method is that it utilizes 3 different approaches to identify the SSL, allowing the machine to be more robust and, thus, be able to more accurately locate the SSL on a variety of ASOCT scans. For ASOCT segmentation, beside a high Dice coefficient, the network also had high sensitivity and specificity, making it a reliable tool in quantifying ASOCT parameters. A comparable algorithm is the STAR Program available on the Casia 2 swept-source ASOCT (Tomey Corporation, Nagoya, Japan), which is capable of automated identification of SSL and ACA measurements[24]. However, this program is a semi-automated software which uses simple edge detection to detect the scleral spur-veva edge line and, from that, detect the scleral spur location[24]. Moreover, it also depends on the assumption that SSL lies in a perfect circle. In cases of narrow angle, there will be iridotrabecular contact and the scleral spur-veva edge line will not be visible. In our approach, the machine is trying to learn from human expertise, hence it can detect the scleral spur without the edge line and it also has the potential to expand its definition of scleral spur implicitly by learning from the expert human grader.

The main limitation in our study was the lack of an absolute ground truth in labelling of the ASOCT images. The labelled data was being prepared by human trainers. This is compounded by crowding of the ACA in eyes with angle closure. The compressed ocular tissues, namely the cornea, peripheral iris and trabecular meshwork, make accurate identification of the scleral spur challenging. Hence, one of the limitations of the paper is the lack of trainers. To validate the machines performance without a true ground truth, we used the inter- and intra-observer test and ICC, with the exception of the ASOCT segmentation where we only had one trainer and observer. Through the validation tests conducted, it was shown that the machine performance was in good agreement with human performance, while the former was more consistent.

As mentioned before, the lack of a generalized population of trainers caused the machines performance to be biased towards the trainers errors. As shown in our inter-observer test, since observer A was a trainer for the network, the distance between machine and observer A was lower than the machine with observer B or C. This limitation could be resolved simply by having more trainers. The second limitation was the presence of only one expert. Again, this could be resolve by having more experts.

One technical limitation of our approach was that the resolution depends on the Focus region. The landmarks could not lie too close to the border. The distance should be larger than half of the focus region length, since the point of interest lay in the center of the region. This could be resolved partially with padding (introduce non-meaningful features) or decreasing the size of focus region (susceptible to class imbalances[17]).

The impact of our method of accurate and automated identification of the scleral spur in ASOCT scans would be in the diagnosis and monitoring of angle closure glaucoma eyes. The diagnosis of angle closure on ASOCT images is dependent on accurate localization of the scleral spur. Angle closure is defined by contact between the peripheral iris and the trabecular meshwork anterior to the scleral spur[21]. As such, the accurate localization of the scleral spur can potentially make screening of angle closure glaucoma on ASOCT imaging easier and more automated. This is especially useful for modern swept-source ASOCT which provides a 360-degree scan of the eye and as many as 64 cross-section cuts of the ACA per eye. The automated identification of the scleral spur reduces variability of human graders and speeds up image analysis to provide a more comprehensive evaluation of the ACA. In the monitoring of angle closure glaucoma eyes, the ACA characteristics should be tracked over time and this paper demonstrates how these parameters can be measured in a reproducible manner, as most ACA measurements use the scleral spur as the reference. These ACA parameters are important in determining the mechanisms of angle closure, guiding clinical management and measuring efficacy of treatment modalities[20, 15].

Disclosures

The authors declare that there are no conflicts of interest related to this article.

References

- [1] RJ Casson, HS Newland, J Muecke, S McGovern, LM Abraham, WK Shein, D Selva, and T Aung. Gonioscopy findings and prevalence of occludable angles in a burmese population: the meiktila eye study. *British journal of ophthalmology*, 91(7):856–859, 2007.
- [2] Sunee Chansangpetch, Prin Rojanapongpun, and Shan C Lin. Anterior segment imaging for angle closure. *American journal of ophthalmology*, 188:xvi–xxix, 2018.
- [3] Jin-Wei Cheng, Ying Zong, You-Yan Zeng, and Rui-Li Wei. The prevalence of primary angle closure glaucoma in adult asians: a systematic review and meta-analysis. *PloS one*, 9(7):e103222, 2014.
- [4] Ricardo J. Cumba, Sunita Radhakrishnan, Nicholas P. Bell, Kundandeeep S. Nagi, Alice Z. Chuang, Shan C. Lin, Kimberly A. Mankiewicz, and Robert M. Feldman. Reproducibility of scleral spur identification and angle measurements using fourier domain anterior segment optical coherence tomography. *Journal of Ophthalmology*, 2012:1–14, 2012.
- [5] Sripad Krishna Devalla, Khai Sing Chin, Jean-Martial Mari, Tin A Tun, Nicholas G Strouthidis, Tin Aung, Alexandre H Thiry, and Michal JA Girard. A deep learning approach to digitally stain optical coherence tomography images of the optic nerve head. *Investigative ophthalmology & visual science*, 59(1):63–74, 2018.
- [6] Sripad Krishna Devalla, Prajwal K Renukanand, Bharathwaj K Sreedhar, Giridhar Subramanian, Liang Zhang, Shamira Perera, Jean-Martial Mari, Khai Sing Chin, Tin A Tun, and Nicholas G Strouthidis. Drunet: a dilated-residual u-net deep learning network to segment optic nerve head tissues in optical coherence tomography images. *Biomedical optics express*, 9(7):3244–3265, 2018.
- [7] Michal Drozdal, Eugene Vorontsov, Gabriel Chartrand, Samuel Kadoury, and Chris Pal. *The importance of skip connections in biomedical image segmentation*, pages 179–187. Springer, 2016.
- [8] Yadollah Eslami, Golshan Latifi, Sasan Moghimi, Reza Ghaffari, Ghasem Fakhraie, Reza Zarei, Mahmood Jabbarvand, Massood Mohammadi, and Shan Lin. Effect of adjunctive viscogonioplasty on drainage angle status in cataract surgery: a randomized clinical trial. *Clinical & experimental ophthalmology*, 41(4):368–378, 2013.
- [9] David S Friedman. Epidemiology of angle-closure glaucoma. *J Curr Glaucoma Pract*, 1(1):1–3, 2007.
- [10] Stuart Geman, Elie Bienenstock, and Ren Doursat. Neural networks and the bias/variance dilemma. *Neural Computation*, 4(1):1–58, 1992.
- [11] Yoseob Han and Jong Chul Ye. Framing u-net via deep convolutional framelets: Application to sparse-view ct. *IEEE transactions on medical imaging*, 37(6):1418–1429, 2018.
- [12] Lars Kai Hansen and Peter Salamon. Neural network ensembles. *IEEE Transactions on Pattern Analysis & Machine Intelligence*, 12(10):993–1001, 1990.
- [13] Mohammad Havaei, Axel Davy, David Warde-Farley, Antoine Biard, Aaron Courville, Yoshua Bengio, Chris Pal, Pierre-Marc Jodoin, and Hugo Larochelle. Brain tumor segmentation with deep neural networks. *Medical image analysis*, 35:18–31, 2017.
- [14] Kaiming He, Xiangyu Zhang, Shaoqing Ren, and Jian Sun. Deep residual learning for image recognition. In *Proceedings of the IEEE conference on computer vision and pattern recognition*, pages 770–778, 2015.

- [15] Victor Koh, Mohammad Reza Keshtkaran, David Hernstadt, Maria Cecilia D Aquino, Paul T Chew, and Chelvin Sng. Predicting the outcome of laser peripheral iridotomy for primary angle closure suspect eyes using anterior segment optical coherence tomography. *Acta ophthalmologica*, 97(1):e57–e63, 2019.
- [16] Xiaomeng Li, Hao Chen, Xiaojuan Qi, Qi Dou, Chi-Wing Fu, and Pheng Ann Heng. H-denseunet: Hybrid densely connected unet for liver and liver tumor segmentation from ct volumes. *arXiv preprint arXiv:1709.07330*, 2017.
- [17] Charles X Ling and Victor S Sheng. *Class imbalance problem*, pages 171–171. Springer, 2011.
- [18] Dimitrios Marmanis, Jan D Wegner, Silvano Galliani, Konrad Schindler, Mihai Datcu, and Uwe Stilla. Semantic segmentation of aerial images with an ensemble of cnns. *ISPRS Annals of the Photogrammetry, Remote Sensing and Spatial Information Sciences*, 3:473, 2016.
- [19] Jessica S Maslin, Yaniv Barkana, and Syril K Dorairaj. Anterior segment imaging in glaucoma: an updated review. *Indian journal of ophthalmology*, 63(8):630, 2015.
- [20] Sasan Moghimi, Rebecca Chen, Nikoo Hamzeh, Nassim Khatibi, and Shan C Lin. Qualitative evaluation of anterior segment in angle closure disease using anterior segment optical coherence tomography. *Journal of current ophthalmology*, 28(4):170–175, 2016.
- [21] Winifred P. Nolan, Jovina L. See, Paul T. K. Chew, David S. Friedman, Scott D. Smith, Sunita Radhakrishnan, Ce Zheng, Paul J. Foster, and Tin Aung. Detection of primary angle closure using anterior segment optical coherence tomography in asian eyes. *Ophthalmology*, 114(1):33–39, 2007.
- [22] Monisha E Nongpiur, Mingguang He, Nishani Amerasinghe, David S Friedman, Wan-Ting Tay, Mani Baskaran, Scott D Smith, Tien Yin Wong, and Tin Aung. Lens vault, thickness, and position in chinese subjects with angle closure. *Ophthalmology*, 118(3):474–479, 2011.
- [23] Monisha E Nongpiur, Lisandro M Sakata, David S Friedman, Mingguang He, Yiong-Huak Chan, Raghavan Lavanya, Tien Yin Wong, and Tin Aung. Novel association of smaller anterior chamber width with angle closure in singaporeans. *Ophthalmology*, 117(10):1967–1973, 2010.
- [24] R. Okamoto, K. & Higashita. Anterior eye three-dimensional image processing apparatus and method of anterior eye three-dimensional image processing., 2017.
- [25] Ying Pan and Rohit Varma. Natural history of glaucoma. *Indian journal of ophthalmology*, 59(Suppl1):S19, 2011.
- [26] Tobias Pohlen, Alexander Hermans, Markus Mathias, and Bastian Leibe. Fullresolution residual networks for semantic segmentation in street scenes. *arXiv preprint*, 2017.
- [27] Natalia Porporato, Mani Baskaran, and Tin Aung. Role of anterior segment optical coherence tomography in angleclosure disease: a review. *Clinical & experimental ophthalmology*, 46(2):147–157, 2018.
- [28] Desmond TL Quek, Monisha E Nongpiur, Shamira A Perera, and Tin Aung. Angle imaging: advances and challenges. *Indian journal of ophthalmology*, 59(Suppl1):S69, 2011.
- [29] H. A. Quigley and A. T. Broman. The number of people with glaucoma worldwide in 2010 and 2020. *The British journal of ophthalmology*, 90(3):262–267, 2006.
- [30] Olaf Ronneberger, Philipp Fischer, and Thomas Brox. U-net: Convolutional networks for biomedical image segmentation. In *International Conference on Medical image computing and computer-assisted intervention*, pages 234–241. Springer, 2015.

- [31] Lisandro M. Sakata, Raghavan Lavanya, David S. Friedman, Han T. Aung, Hong Gao, Rajesh S. Kumar, Paul J. Foster, and Tin Aung. Comparison of gonioscopy and anterior segment ocular coherence tomography in detecting angle closure in different quadrants of the anterior chamber angle. *Ophthalmology*, 115(5):769–774, 2008.
- [32] Lisandro M Sakata, Raghavan Lavanya, David S Friedman, Han T Aung, Steve K Seah, Paul J Foster, and Tin Aung. Assessment of the scleral spur in anterior segment optical coherence tomography images. *Archives of Ophthalmology*, 126(2):181–185, 2008.
- [33] F. E. Seager, J. Wang, K. S. Arora, and H. A. Quigley. The effect of scleral spur identification methods on structural measurements by anterior segment optical coherence tomography. *J Glaucoma*, 23(1):e29–38, 2014.
- [34] Jovina LS See, Maria Cecilia D Aquino, Joel Aduan, and Paul TK Chew. Management of angle closure glaucoma. *Indian journal of ophthalmology*, 59(Suppl1):S82, 2011.
- [35] Pierre Sermanet, David Eigen, Xiang Zhang, Michal Mathieu, Rob Fergus, and Yann LeCun. Overfeat: Integrated recognition, localization and detection using convolutional networks. *arXiv preprint arXiv:1312.6229*, 2013.
- [36] Shai Shalev-Shwartz and Shai Ben-David. *Understanding machine learning: From theory to algorithms*. Cambridge university press, 2014.
- [37] Chelvin C Sng, John C Allen, Monisha E Nongpiur, Li-Lian Foo, Yingfeng Zheng, Carol Y Cheung, Mingguang He, David S Friedman, Tien Y Wong, and Tin Aung. Associations of iris structural measurements in a chinese population: the singapore chinese eye study. *Investigative ophthalmology & visual science*, 54(4):2829–2835, 2013.
- [38] Christian Szegedy, Alexander Toshev, and Dumitru Erhan. Deep neural networks for object detection. In *Advances in neural information processing systems*, pages 2553–2561, 2013.
- [39] A. N. Tan, L. D. C. Sauren, J. de Brabander, T. T. J. M. Berendschot, V. L. Passos, C. A. B. Webers, R. M. M. A. Nuijts, and H. J. M. Beckers. Reproducibility of anterior chamber angle measurements with anterior segment optical coherence tomography. *Investigative Ophthalmology & Visual Science*, 52(5):2095–2099, 2011.
- [40] Yih-Chung Tham, Xiang Li, Tien Y. Wong, Harry A. Quigley, Tin Aung, and Ching-Yu Cheng. Global prevalence of glaucoma and projections of glaucoma burden through 2040: a systematic review and meta-analysis. *Ophthalmology*, 121(11):2081, 2014.
- [41] Dandan Wang, Meng Qi, Mingguang He, Lingling Wu, and Shan Lin. Ethnic difference of the anterior chamber area and volume and its association with angle width. *Investigative ophthalmology & visual science*, 53(6):3139–3144, 2012.
- [42] Ren-Yi Wu, Monisha E Nongpiur, Ming-Guang He, Lisandro M Sakata, David S Friedman, Yiong-Huak Chan, Raghavan Lavanya, Tien-Yin Wong, and Tin Aung. Association of narrow angles with anterior chamber area and volume measured with anterior-segment optical coherence tomography. *Archives of ophthalmology*, 129(5):569–574, 2011.
- [43] Bing Xu, Naiyan Wang, Tianqi Chen, and Mu Li. Empirical evaluation of rectified activations in convolutional network. *arXiv preprint arXiv:1505.00853*, 2015.
- [44] Jun Zhang, Mingxia Liu, and Dinggang Shen. Detecting anatomical landmarks from limited medical imaging data using two-stage task-oriented deep neural networks. *IEEE Transactions on Image Processing*, 26(10):4753–4764, 2017.

- [45] Zengni Li, Ahmed Abdulkadir, Soeren S. Lienkamp, Thomas Brox, and Olaf Ronneberger. 3d u-net: learning dense volumetric segmentation from sparse annotation. In *International Conference on Medical Image Computing and Computer-Assisted Intervention*, pages 424–432. Springer, 2016.